EFFECTS OF TITANIUM, CERIUM OR ALUMINUM ADDITION ON MICROSTRUCTURE AND MECHANICAL PROPERTIES OF DUCTILE IRON CASTINGS

Mingzhi Xu, Jingjing Qing and Shelton Fowler
Georgia Southern University, Statesboro, GA, USA

https://doi.org/10.1007/s40962-024-01271-2

Abstract

Fineness of microstructural constituents in the metallic alloys affects their mechanical properties. This study sought to determine the effects of selected levels of titanium, cerium and aluminum on the fineness of microstructural constituents within ductile iron. A hypoeutectic iron was studied. Cerium additions in the amounts of 0.01 wt.% and 0.03 wt.%, titanium additions in the amounts of 0.02 wt.% and 0.04 wt.%, and aluminum addition at the amount of 0.02 wt.% were tested. The influences of the selected additions were determined using three methods: direct secondary dendrite arm spacing (SDAS) measurement, liquidus recalescence analysis and tensile testing. The results of the study showed that at above a critical value, cerium refined the SDAS effectively within a distance of 22 mm from the casting bottom surface, whereas for the locations with slower cooling rates, Ce did not refine microstructure and impaired elongation. Titanium had an adverse effect on refining the microstructure when Al-containing inoculant was used. The addition of Al was found effective at achieving a refined microstructure and improved mechanical properties. The inclusion composition and number density change as a result of alloy additions were measured.

Keywords: *ductile iron, fineness, microstructure, mechanical properties, cerium, titanium, aluminum additions*

Introduction

Ductile iron (DI) is the most commonly used type of cast iron for structural components due to a combination of high tensile strength and high ductility.[1] The graphite shape in DI is spherical/nodular and a micrograph of DI is shown in Figure 1. The formation of the nodular graphite leads to a higher elongation than the gray iron (GI) with flaky graphite because the rounded graphite nodules reduce stress concentrations and inhibits crack formation and propagation.[1] The trade-off of the different graphite shapes is that DI has far less capacity for vibration dampening and a lower heat transfer rate than GI. In addition, ductile iron has a high tendency for solidification shrinkage.[2,3]

While ductile iron gets most of its ductility from the presence of nodular graphite, the ultimate tensile strength is far more reliant on the iron matrix around the graphite particles. The phases, including pearlite, ferrite, martensite, austenite or ausferrite, in the ductile iron matrix are transformation products of austenite. Fineness of the matrix phases is directly related to the fineness of austenite. This is where austenite refinement can largely impact the overall strength of a ductile iron casting. In hypoeutectic irons and some steels (C>0.52 wt.%), the primary phase that forms in the liquid is known as austenite.[4,5] Austenite is a high-temperature solid solution phase of carbon and iron that is typically unstable at room temperature, except in instances of high cooling rate or addition of alloying elements that stabilize the austenite, for example in austenitic stainless steels. Austenite is the precursor to several other phases which depend on the cooling rate. This means that the refinement of austenite directly correlates to a finer structure in the final casting.[6]

Heterogeneous nuclei for nucleating the new phase can lower the free energy and undercooling of forming new

This paper is an invited submission to IJMC selected from presentations at the 7th Keith Millis Symposium on Ductile Iron held October 18–20, 2023, at the Crown Plaza Atlanta Perimeter at Ravinia, Atlanta, GA. It is published in the IJMC by permission of the DIS (Ductile Iron Society).

Received: 27 December 2023 / Accepted: 12 January 2024 / Published online: 19 February 2024

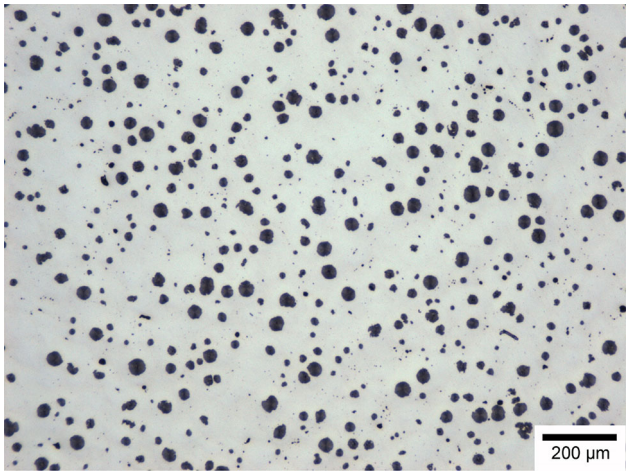

Figure 1. Spheroidal graphite in a ductile iron.

phase. A higher population of heterogeneous nuclei will lead to a higher population of dendrites, so as a finer grain structure. Alloy additions that form appropriate compounds may create a 'seed' for the austenite to grow on[7]; this reduces undercooling as the nucleation point already exists in the liquid and does not have to be formed. It is possible for austenite to homogeneously nucleate, but a higher undercooling of the liquid metal is necessary as the nucleation point must form from the liquid metal. Heterogeneous nucleation elements/compounds need to have specific properties to properly work. Ideally, the nucleation compound will have a similar crystal structure or good crystallographic lattice matching (low lattice disregistry) to the phase to be nucleated.[5] Often the element added forms an oxide, carbide or nitride compound with other elements present in the liquid which then in turn acts as the heterogeneous nucleation site.[8] The nucleation agent must also be solid at the solidification temperature of the liquid metal, and it must be able to be wetted by the liquid metal[9,10]

In a hypoeutectic iron, austenite forms structures known as dendrites during solidification. The basic morphology that the austenite exhibits during solidification is shown in Figure 2. It is challenging to directly observe the size of

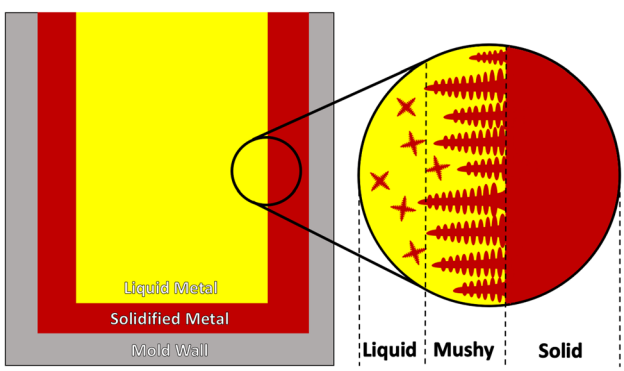

Figure 2. Dendrite structure at solidification front.

austenite grains in the as-cast ductile irons, because austenite is not stable at room temperature in most alloys. However, the transformation of austenite still retains the shape of the dendrites, making it possible to trace back the original austenite dendrite structure. Secondary dendrite arm spacing (SDAS) of austenite dendrite is used in this study to assess the fineness of austenite. The secondary arm spacing of dendrites is inversely related to the cooling rate of a casting.[11]

The SDAS impacts the mechanical properties of the casting.[12–14] As the SDAS is reduced, properties such as hardness, ultimate tensile strength and yield strength of the material improve.[15] The refinement of the microstructure is of great interest to the ferrous metals industry. Previous studies have well investigated the refinement of graphite nodules in the ductile irons, [16–19] but effects of Ce, Al and Ti additions on the SDAS in DI was not well documented.

Rare earth elements are well known for their ability to form compounds and refine grains in steel, although the exact mechanism is not well understood. The predominant theory is that rare earths form various oxides and sulfides which are solid at high temperatures and which match closely with the crystal structure of austenite. The ability of these compounds to nucleate austenite is quite inconsistent though across different studies.[9] One study found that cerium readily formed oxides, sulfides and oxy-sulfides which did successfully reduce the austenite grain size, although additions above 0.15 wt.% promoted the formation of a large amount of inclusions.[20] Another study that assessed the effects of cerium addition saw very little change in the size of austenite with a 0.05 wt.% addition, but when a 0.1 wt.% addition was performed in mold, the grain size was drastically reduced. The addition of cerium in this study was also noted to have promoted more equiaxed grains, meaning that the modification of the grain size was more effective. This study did also note the intermetallic inclusions seen in the previous study.[21]

Several studies have reported that titanium is an effective element for refining austenite in steel, gray iron and ductile iron. One study investigated the effects of titanium addition on the grain size of S45C carbon steel at concentrations up to 0.5 mol%.[22] The mechanism of grain refinement in this case was apparently not due to heterogeneous nucleation, but rather due to the pinning of austenite grains at interdendritic regions by TiC and TiN particles. A similar study theorized that TiC and TiN did act as heterogeneous nuclei in high Mn steel.[23] This study found austenite grain size decrease by up to 37%, as well as significant property improvements. One study found that titanium was effective in refining austenite dendrites in thin walled, high nickel ductile iron castings.[24] This study explored the effects of titanium addition up to a concentration of 0.13 wt.% and found that titanium was more effective than Nb and Zr at refining proeutectic austenite. Another cast iron study

found that the addition of titanium led to a reduction of mechanical properties in gray cast iron.[25] In this study concentrations between 0.013 to 0.031 wt.% titanium was added to gray iron to assess the effect on mechanical properties. The mechanism of weakening proposed by this study was that titanium readily forms TiN which in turn removes free nitrogen from the melt. According to the authors, nitrogen is beneficial to the nucleation of austenite in gray iron and the removal of it increased grain size.[25]

This study explores the effects of cerium, titanium and aluminum on microstructural fineness (SDAS and fineness of graphite nodules) as well as tensile properties in a ductile iron. This study also investigates the additions effects on the finesses of microstructure with different cooling rates.

Design of Experiments

Alloy Composition and Test Matrix

The target composition for the major elements in the ductile iron is listed in Table 1. This composition was initially designed to retain the original austenite structure for direct grain size observation through a hot shakeout and quench process. The Ni and Mo were added to suppress the transformation of austenite during the shakeout and quench. After the trial heats, it was found that the quench was not able to retain the austenite reliably across the casting. However, the addition of Ni and Mo helps to enhance the contrast for identifying dendritic structure when etching the metallographic samples, so the original compositions were used for the rest of the study. The targeted composition produces a hypoeutectic ductile iron, with the austenite as the primary phase during the solidification.

The primary additive elements of interest in this study include Al, Ce and Ti. The concentrations of additive elements were varied to investigate their effects on the microstructure. The starting contents of the three additive elements were chosen based on the previous studies.[6,8,14,22] Two commercially available inoculants (Inoculant 1 containing Al and Inoculant 2 containing Al and Ce) and a common nodulizer were used, and their compositions can be found in Table 2. The heat using Inoculant 1 without Ce or Ti or additional Al was used as the baseline. Titanium and cerium additives were introduced in addition to Inoculant 1 in the subsequent heats to investigate their effects. Inoculant 2 with lower aluminum content than Inoculant 1 was used to study the effect of additional aluminum in the ductile iron. Detailed combinations of inoculant and elemental additives used across different heats are listed in Table 3.

Table 1. Concentration of Major Elements in the Ductile iron Selected for This Study

Element	C	Si	CE	Mn	Ni	Mo
Wt. %	3.5	2.0	4.17	1.0	1.0	0.1

Heat Procedure

The heat procedure was kept as consistent as possible across seven heats. The 100-lb induction furnace was charged based on a calculated charge table (Table 4) to achieve the target composition for the ductile iron. The heat was started by charging only high purity pig iron and steel in the furnace without protective gas (air melting). After the initial charge materials have become molten, FeMn, Ni, FeMo and FeSi were added into the furnace and allowed to dissolve. Subsequently, a chilled chemistry sample was taken from the furnace and then analyzed using an optical emission spectrometer and a carbon/sulfur combustion analyzer to ensure that the chemistry was close to the target before pouring. Further chemistry trim was performed prior to tapping whenever was needed. Once the melt reached a temperature of 1430 °C, the metal was tapped into a 100-lb ladle that had been thoroughly preheated. The inoculant, the nodulizer and Ce/Ti/Al addition (if any) were added to the bottom of the ladle and loosely covered with steel sheets to keep the additions from

Table 2. Compositions of Two Commercial Inoculants and Nodulizer Used in this Study

wt. %	Si	Ca	Al	Ce	Mg	RE
Inoculant 1	73.09	0.96	0.97	1.84	–	–
Inoculant 2	66.63	0.97	4.15	–	–	–
Nodulizer	45.99	0.804	0.462	–	5.71	0.01

Table 3. Test Matrix: Inoculant and Elemental Additives Used in Different Heats

Heat 1	Inoculant 1
Heat 2	Inoculant 2
Heat 3	Inoculant 2 + 0.01 wt.% Ce
Heat 4	Inoculant 2 + 0.03 wt.% Ce
Heat 5	Inoculant 2+ 0.02 wt.% Ti
Heat 6	Inoculant 2 + 0.04 wt.% Ti
Heat 7	Inoculant 1 + 0.02 wt.% Al

floating for the higher treatment recoveries. The inoculation rate was 0.15 wt% of the total weight of heat. The amount of nodulizer used was calculated for producing a final magnesium content of 0.040–0.045 wt.%.

Mold and Casting

Because microstructure refinement positively impacts material properties, tensile testing was adopted to verify if the refinement had improved the DI's tensile properties. A 1-inch Y-block geometry following ASTM A536 was adopted to produce castings for DI tensile bars. The mold was designed with a bottom filling gating system to reduce filling velocity and improve casting quality. Four Y-blocks were arranged in a single mold, so that they could be filled simultaneously to produce four equivalent castings. The Y-block geometry and gating design were shown in Figure 3. For each heat where four Y-blocks were produced, one of the Y-block will be sectioned for metallographic samples, another Y-block would be sectioned to machine two tensile bars from the casting. Filling and solidification simulation results for the mold design showed a smooth, low velocity filling with no major macroporosity in the region for sampling DI tensile bars, as given in Figure 4.

Table 4. Charge Table Used to Produce the Ductile Iron with Targeted Composition

Material	Charge amount (kg)	Charge amount (lbs)
High purity pig iron	25.6	56.32
Steel scrap (1018)	4.49	9.878
FeMn	0.450	0.99
Ni	0.32	0.704
FeMo	0.045	0.099
FeSi (75%)	0.499	1.0978
Nodulizer (ladle)	0.405	0.891
Inoculant (ladle)	0.0476	0.10472
Total charge	31.9	70.18

Metallography and Microstructure Analysis

For each heat, two metallographic samples were cut from the center of a Y-block at the equivalent locations where the tensile bars were cut, as shown in Figure 5. The metallographic samples were polished following standard metallographic sample preparation procedure, and they were examined using an optical microscope under the as-polished/unetched and the etched (with 2% Nital) conditions. Microstructure images in unetched condition from all heats performed are shown in Figure 6(a)–(g). Each sample was approximately one inch in height and three quarters of an inch wide. Micrographs of each sample were captured along the middle of the section from the top to the bottom. This allowed for the measurement of phases in the microstructure at designated distances from the surface of the casting. The ability to capture micrographs from locations of a range of cooling conditions was important as fineness of microstructure is related to the cooling rate; this also allows for a good representation of the microstructural fineness in the entire tensile testing region. Nital (2 vol.%) etching was able to reveal the ferrite rims around the graphite nodules, and the rest of the matrix was pearlite. Segregation of alloys in this ductile iron alloy was helping with the delineation of dendritic structure in the matrix, as shown in Figure 6(h). ImageJ software was used to perform image analysis of the micrographs (captured at 100× magnification) of the etched samples under various conditions, when measurements SDAS and graphite size were quantitatively performed. Lines perpendicular to dendrite arms were drawn using ImageJ, and the lengths of lines were recorded. Number of dendrite arms that the lines passed through were counted. A minimum of 30 dendrite arms were used for the SDAS measurement in each region. For each region the total length of all lines was summed and then divided by the total number of dendrite arms crossed to calculate the average SDAS. A demonstration of the length measurement using the ImageJ

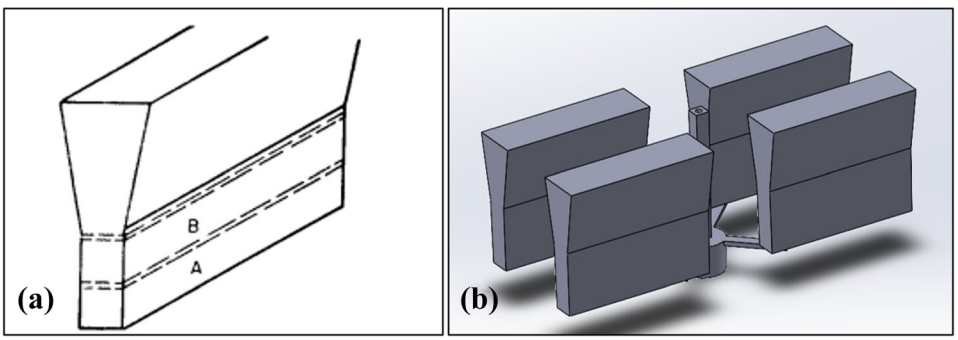

Figure 3. Schematics of (a) ASTM A536 Y-block geometry (b) arrangement of Y-blocks in a single mold.

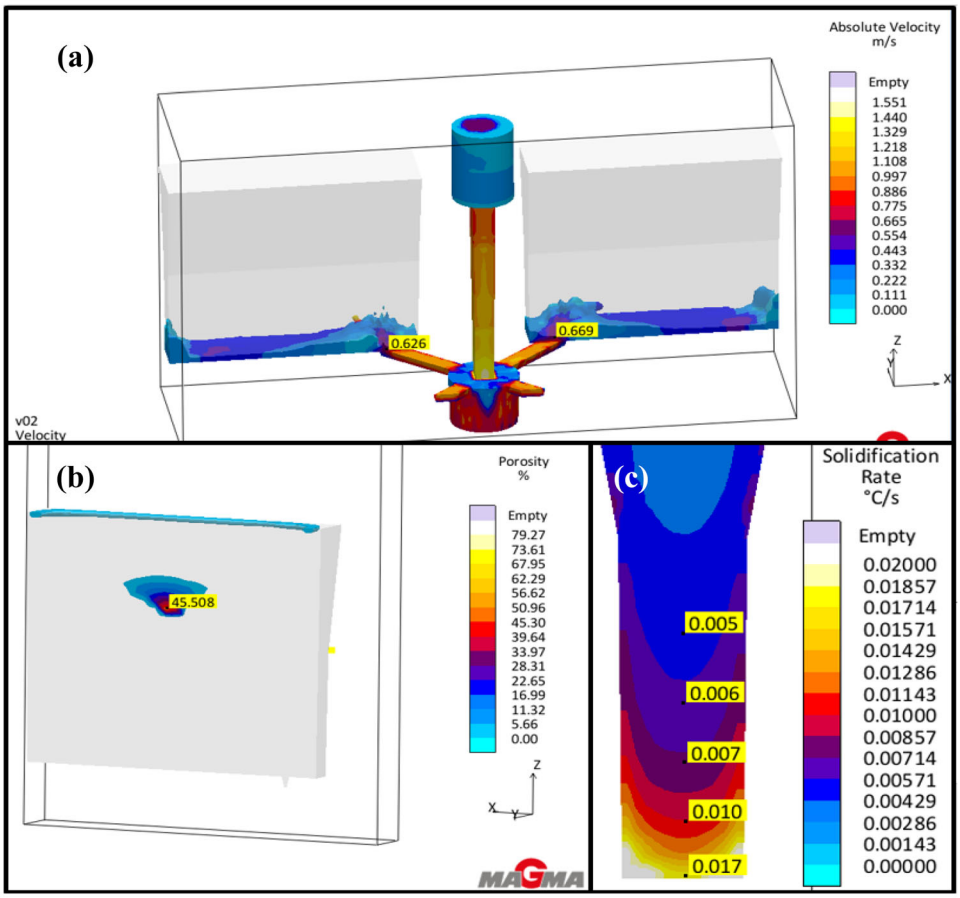

Figure 4. Filling and solidification simulation results showing: (a) filling velocity at the ingate to the Y-block mold (only two out of the four Y-blocks are shown here); (b) porosity in a keel block and the tensile bars were machined at the region 1-2 in. from bottom of the Y-block; (c) solidification rate in the region of sampling tensile bars in a Y-block.

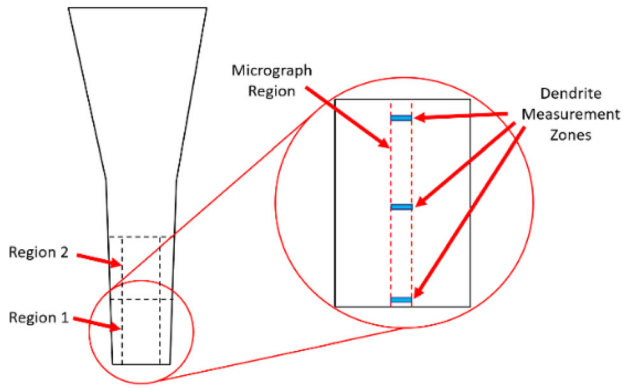

Figure 5. Y-block cross section and microstructure examination area.

software is also shown in Figure 6, with the red lines used for the measurement. A scanning electron microscope (SEM) equipped with automated feature analysis (AFA) was utilized for the graphite size distribution measurement and nonmetallic inclusion characterization using the as-polished metallography samples.

Thermal Analysis

Thermal analysis is a sensitive method to detect phase transformation during solidification and cooling. Alloy studied is a hypoeutectic ductile iron, and austenite is the primary phase that forms during solidification. Undercooling is the driving force for nucleation during solidification. Recalescence during phase transformation may be used to assess the phase transformation, and a small recalescence at the liquidus temperature indicates a better nucleation of austenite. A cylindrical insulating sleeve measuring 2.5” internal diameter by 6” in height and 3/8” in thickness was imbedded in a no-bake mold to produce another casting geometry which would be cooled at a slower cooling rate than the Y-blocks, as shown in Figure 7. The slowed cooling rate and prolonged solidification time helped with easier identification of thermal arrests during thermal analysis. A thin tipped thermocouple was placed through the wall of the mold so that the tip was in the center of the mold cavity. This mold was then poured alongside each of the Y-block sets for each heat, and the cooling data were recorded using a data acquisition system.

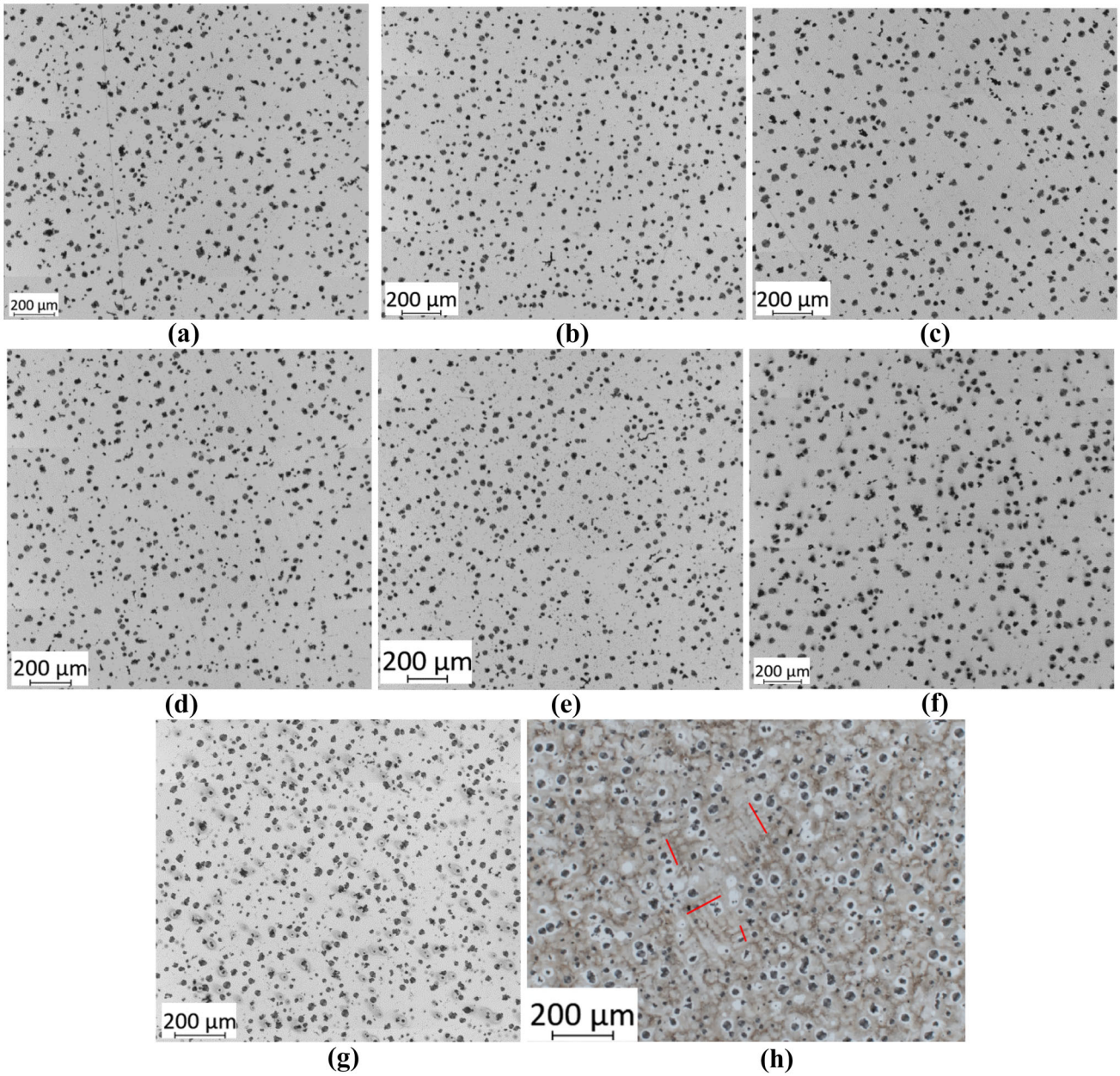

Figure 6. Unetched microstructure from sections 11mm away from Y-block bottom surface in heats 1 (a), 2 (b), 3 (c), 4 (d), 5 (e), 6 (f), 7 (g); and a sample measurement of the SDAS in a region from heat 2 (h).

Tensile Testing

Three tensile bars were machined from the Y-blocks from locations as shown in Figure 3(a) for each heat, and the tensile testing was performed according to ASTM A370 standards. An extensometer was attached to the sample for the first 1% of elongation before being removed and the crosshead displacement being used instead. The yield strength was determined using the 0.2% offset method as specified by ASTM A370. The ultimate tensile strength (UTS) is the maximum stress experienced by the tensile specimen. The elongation was also determined from the stress–strain data.

Results

Heat Chemistry

The chemistry determined using OES for each heat are listed in Table 5. Variation of chemistry across different heats was not significant, and Al/Ti/Ce levels were varied due to the elemental additions.

Secondary Dendrite Arm Spacing and Nodule Size Distribution

The SDAS as a function of the distance the bottom casting wall in the test region is shown in Figure 8. In general, the SDAS was smallest at the casting surface, and it increases as the distance furthers due to the slower solidification rates. A more detailed comparison between different heats can be found in "Discussions" section. A scanning electron microscope (SEM) equipped with EDX (energy-dispersive X-ray) detector and auto feature analysis (AFA) software was utilized to perform statistical analysis of large quantity of graphite nodules and nonmetallic inclusions in the matrix across the different samples. Detailed principles and applications of SEM–AFA can be found in reference.[26]

The count of graphite nodules as well as graphite nodule size were measured in samples from heats 2, 4, 6 and 7 at sections 11mm from bottom casting wall using SEM–AFA. The nodule counts for the designated sections of heats 2, 4, 6 and 7, as well as inclusions number density are provided in Table 6. The distributions of graphite size are shown in Figure 9. It was observed that the type of alloy addition influences the size distribution of graphite nodules, but further analysis is still in progress and will be reported in the future. Nonmetallic inclusions in the matrix were also statistically analyzed using the SEM–AFA function.

Liquidus Recalescence

Thermal analysis of each cooling curve was performed. Taking heat 1 as an example, the cooling curve was plotted with its first and second derivatives in Figure 10. The cooling curve shows a slight amount of undercooling at the liquidus transition. The minimum temperature at liquidus occurs at the point where the first derivative first crosses zero; the temperature at this point is 1169.14 °C. The maximum liquidus temperature occurs at the time the first derivative next crosses zero; in this case the maximum temperature is 1169.47 °C. The difference between these two temperatures is the calculated recalescence at the liquidus temperature. All the heats were analyzed using the same method to acquire the high and low temperatures at

Figure 7. Insulated mold made with an insulation sleeve and no-bake sand used for thermal analysis.

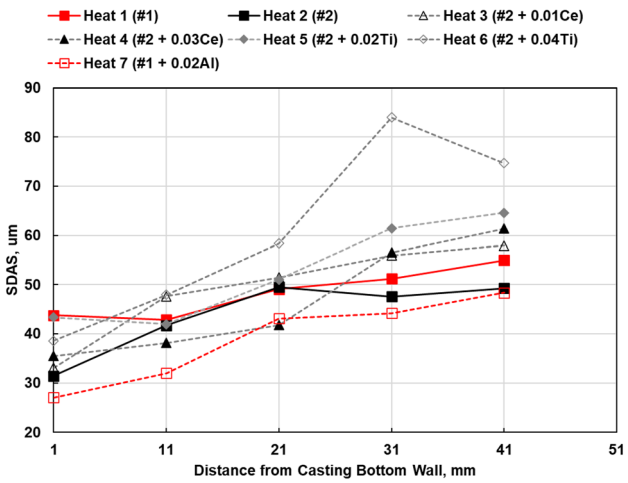

Figure 8. SDAS versus distance of the sampling location from the bottom casting wall for each heat.

Table 5. Chemistry of Ductile Irons in the Different Heats

Sample #	Inoculant and additions	C	Si	CE	Mn	Mo	Ni	Al	Ti	Ce	Mg
Target	Vary	3.50	2.00	4.17	1.00	0.15	1.00	–*	–	–	0.045
Heat 1	Inoculant 1	3.48	1.97	4.14	1.08	0.17	1.08	0.007	0.012	0.010	0.043
Heat 2	Inoculant 2	3.45	2.06	4.13	1.05	0.16	1.07	0.015	0.011	–	0.042
Heat 3	Inoculant 2+ 0.01 wt.% Ce	3.37	2.08	4.06	1.08	0.16	1.03	0.012	0.010	0.010	0.040
Heat 4	Inoculant 2+ 0.03 wt.% Ce	3.55	2.10	4.25	1.09	0.16	1.04	0.012	0.011	0.028	0.043
Heat 5	Inoculant 2 + 0.02 wt.% Ti	3.34	2.07	4.03	1.07	0.15	1.05	0.014	0.028	–	0.040
Heat 6	Inoculant 2 + 0.04 wt.% Ti	3.38	2.00	4.05	1.01	0.16	1.03	0.013	0.048	–	0.045
Heat 7	Inoculant 1 + 0.02 wt.% Al	3.42	1.94	4.07	1.01	0.17	1.00	0.023	0.012	–	0.046

*Below detection limit

Table 6. Graphite Nodule Count in Selected Heats Measured at Sections 11 mm from the Bottom Casting Wall

Heat #	Inoculant and alloy addition	Nodule count, #/mm^2	Inclusion number density, #/mm^2			
			Nitrides	Sulfides	Oxides	Total
Heat 2	Inoculant 2	148.6	119.2	65.7	981.7	1,166.6
Heat 4	Inoculant 2 + 0.03Ce	165.7	155.0	116.7	1183.1	1,454.8
Heat 6	Inoculant 2 + 0.04Ti	94.0	238.5	36.9	604.8	880.3
Heat 7	Inoculant 1 + 0.02Al	134.2	259.6	128.4	761.4	1,149.4

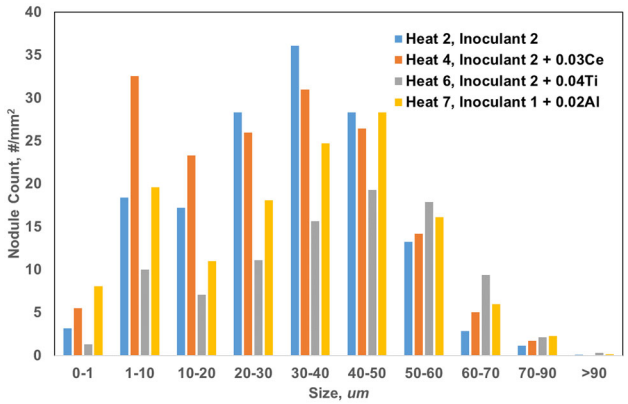

Figure 9. Graphite nodule size distributions measured by SEM-AFA at the sections 11 mm from the bottom casting surface for heats 2, 4, 6 and 7.

liquidus. The calculated liquidus recalescence is listed in Table 7. It can be seen that heats 1 and 2 had identical recalescence, and different alloying additions had different impacts on the recalescence. A more detailed comparison between different heats can be found in "Discussions" section.

Table 7. Liquidus Recalescence (R) for Each Heat

	Inoculant and additions	R(°C)
Heat 1	Inoculant 1	0.33
Heat 2	Inoculant 2	0.33
Heat 3	Inoculant 2 + 0.01 wt.% Ce	0.52
Heat 4	Inoculant 2 + 0.03 wt.% Ce	0.27
Heat 5	Inoculant 2 + 0.02 wt.% Ti	0.94
Heat 6	Inoculant 2 + 0.04 wt.% Ti	0.93
Heat 7	Inoculant 1 + 0.02 wt.% Al	<0.20

Tensile Testing and Material Properties

Tensile properties of samples from the different heat are listed in Table 8. Heats 1 and 2 produced DI castings with similar tensile properties. It was seen that the addition of Al raised both UTS and elongation, but not for the heats with Ce or Ti additions. A more detailed comparison between different heats can be found in "Discussions" section.

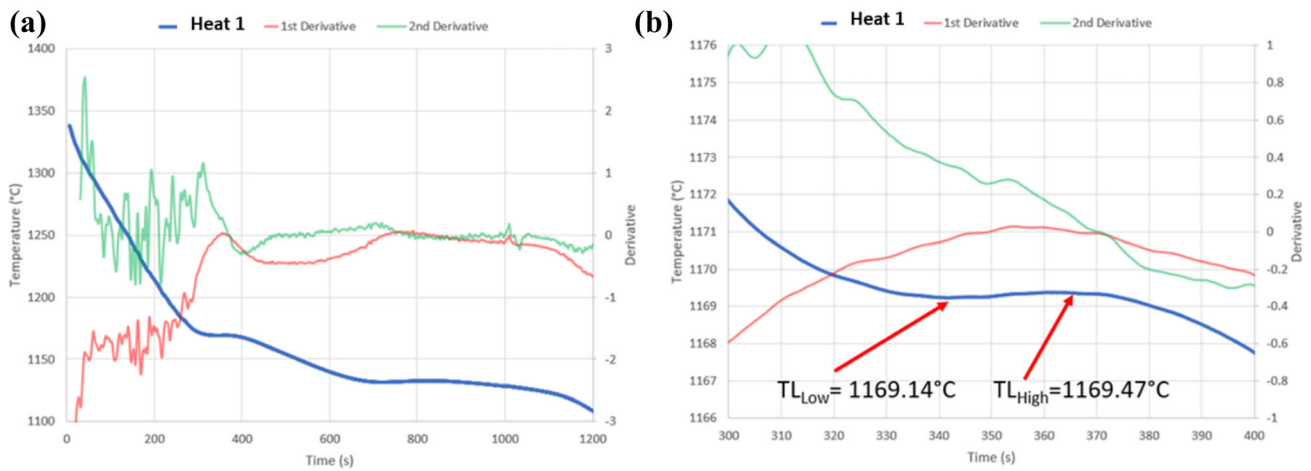

Figure 10. Cooling curve of heat 1 with 1st and 2nd derivatives (a); A magnified view near the liquidus region of the heat 1 cooling curve (b).

Table 8. Tensile Properties of Heats with Different Inoculant and Alloy Combinations

		UTS, ksi	Yield, ksi	Elong. %
Heat 1	Inoculant 1	105.82 ± 0.50	62.37 ± 0.67	9.92 ± 0.42
Heat 2	Inoculant 2	106.80 ± 0.80	60.64 ± 0.36	9.49 ± 0.82
Heat 3	Inoculant 2 + 0.01 wt.% Ce	111.01 ± 0.23	63.98 ± 0.48	7.93 ± 0.42
Heat 4	Inoculant 2 + 0.03 wt.% Ce	112.83 ± 0.48	65.49 ± 0.67	7.33 ± 0.09
Heat 5	Inoculant 2 + 0.02 wt.% Ti	107.34 ± 0.36	61.84 ± 0.65	8.99 ± 1.20
Heat 6	Inoculant 2 + 0.04 wt.% Ti	107.71 ± 0.79	61.72 ± 0.31	8.64 ± 1.31
Heat 7	Inoculant 1- + 0.02 wt.% Al	109.19 ± 0.24	61.70 ± 0.75	10.23 ± 0.55

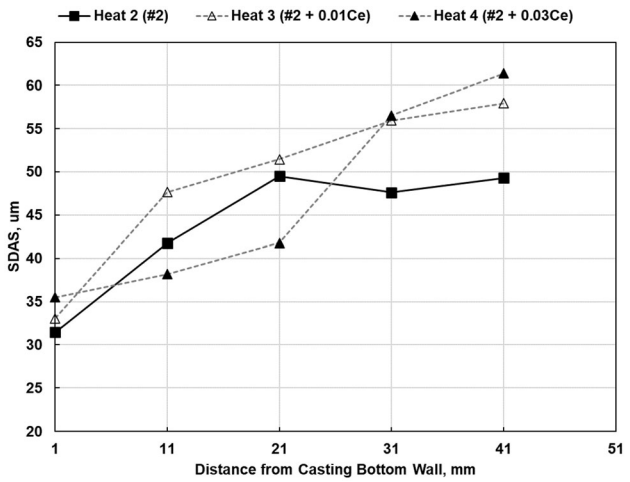

Figure 11. SDAS versus distance of the sampling location from the bottom casting wall for Ce modified heats.

Discussions

The Effect of Cerium Addition

The effect of Ce on the microstructure and mechanical properties can be seen from heats 2, 3 and 4. SDAS data plotted in Figure 11 show clear trends, and contributions of factors influencing fineness of austenite dendrite arms can be assessed using the data. Firstly, the 0.03 wt.% Ce addition in heat 4 had a noticeable effect on the fineness of the secondary dendrite arms for sections within 22 mm from the bottom casting wall. However, at the lower level of 0.01 wt.%, the Ce slightly increased the SDAS. This potentially indicates that there is a critical value of Ce to form enough heterogeneous nucleation sites to effectively nucleate austenite. The liquidus recalescence data in Tables 7 and 9 support this theory. However, at slower cooling rate (30mm or further from casting bottom wall), the SDAS saw an increase of over 20% with the addition of Ce. SEM-AFA analysis (Figure 12) indicated that when Ce was added, comparing heats 4 to heat 2, the density for sulfide inclusions was almost doubled, and the formation of Mg-containing sulfides was significantly suppressed. Instead, the majority of the sulfides were rich in Ce in heat 4. In addition, Ce also promoted formations of oxide inclusions (Figure 13). As shown in Table 6, the overall inclusion density of heat 4 was 30% higher than that of heat 2. Such large amount of inclusion density negatively impacted the elongation of the cast tensile bar, when comparing to heat 2, even though a higher nodule count and overall finer nodule sizes were observed in heat 4.

The Effect of Titanium Addition

The effect of Ti on the microstructure and mechanical properties can be seen from heats 2, 5 and 6. There was a noticeable trend regarding the dendrite arm spacing. For heats 5 and 6, the addition of Ti into an Al-containing inoculant (inoculant #2) coarsened the SDAS, as shown in

Table 9. Liquidus Recalescence and Tensile Properties of Heats with Difference Ce Additions

		Liquidus recalescence (°C)	UTS, ksi	Yield, ksi	Elong. %
Heat 2	Inoculant 2	0.33	106.80 ± 0.80	60.64 ± 0.36	9.49 ± 0.82
Heat 3	Inoculant 2 + 0.01 wt.% Ce	0.52	111.01 ± 0.23	63.98 ± 0.48	7.93 ± 0.42
Heat 4	Inoculant 2 + 0.03 wt.% Ce	0.27	112.83 ± 0.48	65.49 ± 0.67	7.33 ± 0.09

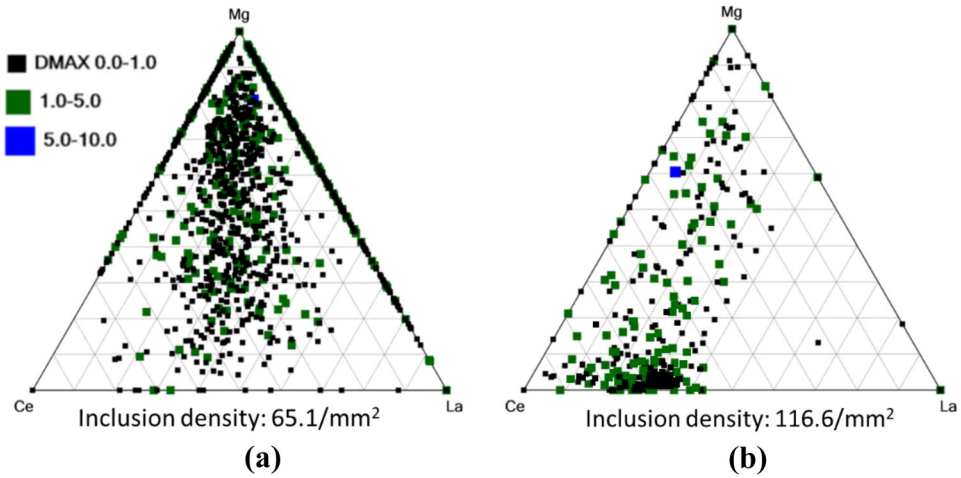

Figure 12. Ternary diagram for sulfide inclusions in (a) heat 2 over a scan area of 29.35 mm² and (b) heat 4 over a scan area of 18.63mm².

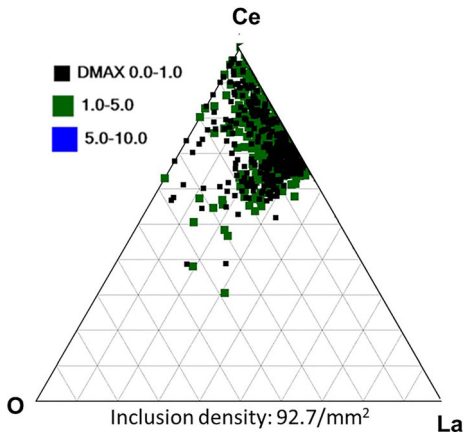

Figure 13. Ternary diagram for Ce- and La-containing inclusions in heat 4 over a scan area of 18.63mm².

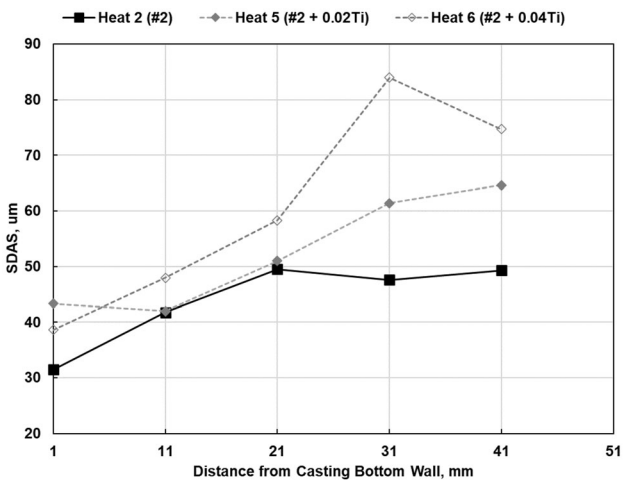

Figure 14. SDAS versus distance of the sampling location from the bottom casting wall for Ti modified heats.

Figure 14. This coarsening effect was even more severe for slower cooling rate (>30 mm from casting bottom surface). Analysis of nonmetallic inclusions shown in Figure 15 suggested that most of nitrides in the castings in heat 2 were complex inclusions rich in Si, Mg and Ti, while the addition of Ti in heat 6 significantly pushed the composition of nitrides to be Ti and Al rich. This reduced the formation of MgAlSi nitrides, which has been found effective in nucleating the austenite.[26–28] The increase of liquidus recalescence with Ti additions in Table 10 also potentially implied the suppression of austenite nucleation due to the addition of Ti. Further thermodynamic calculations would be necessary to determine the inclusion formation sequence during metal solidification to better understand this phenomenon. In addition to the suppression of nucleation, another study claimed that the additional titanium in solution slows down austenite growth and causes a coarser grain structure.[13] When comparing the mechanical properties of heats 5 and 6 with heat 2, UTS and yield strength were found to be similar, but the elongation was reduced slightly. This is possibly due to the formation of cuboidal TiN and AlN inclusions acting as stress concentrators. It should also be noted that Ti addition reduced the nodule count by nearly 40%, and graphite nodule sizes were significantly coarsened. However, the mechanical property of the tensile bar was found similar to that for heat 2. This was possibly due to (1) an overall lower inclusion number density when comparing heat 6 to heat 2 (880/mm^2 vs 1,166/mm^2), as shown in Table 6, and (2) the lower carbon equivalent in heat 6 compared to heat 2.

The Effect of Aluminum Addition

When comparing the effect of Ti on microstructure of ductile iron, the authors found out that Al from inoculant-2 could be effective in refining the microstructure, as shown

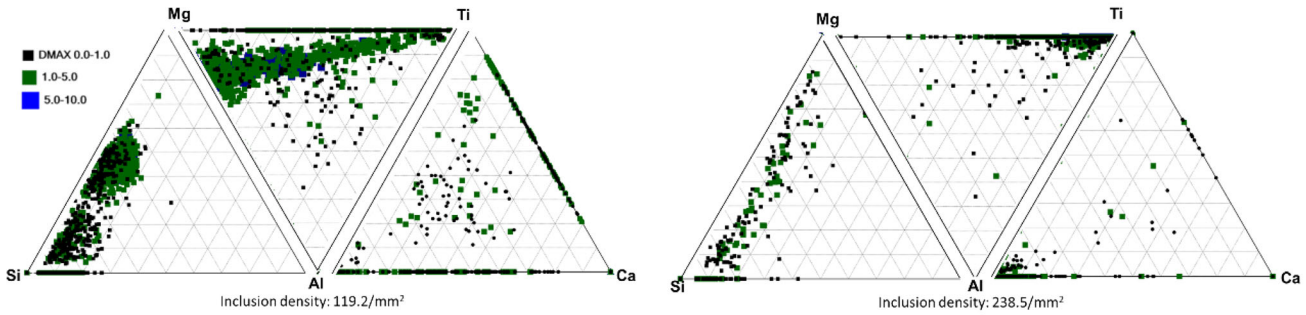

Figure 15. Ternary diagram for nitride inclusions in (a) heat 2 over a scan area of 29.35 mm^2 and (b) heat 6 over a scan area of 10.02 mm^2.

Table 10. Liquidus Recalescence and Tensile Properties of Heats with Difference Ti Additions

		Liquidus recalescence (°C)	UTS, ksi	Yield, ksi	Elong. %
Heat 2	Inoculant 2	0.33	106.80 ± 0.80	60.64 ± 0.36	9.49 ± 0.82
Heat 5	Inoculant 2 + 0.02 wt.% Ti	0.94	107.34 ± 0.36	61.84 ± 0.65	8.99 ± 1.20
Heat 6	Inoculant 2 + 0.04 wt.% Ti	0.93	107.71 ± 0.79	61.72 ± 0.31	8.64 ± 1.31

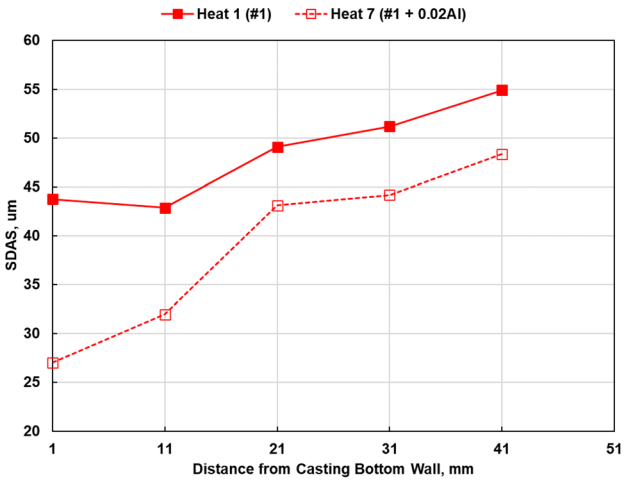

Figure 16. SDAS versus distance of the sampling location from the bottom casting wall for Al modified heats.

in Figure 16 and Table 11, thus heat 7 was performed to verify the hypothesis. The effect of Al on the microstructure and mechanical properties can be seen from heats 1 and 7. At 0.02 wt.% residue Al in the melt in heat 7, the SDAS was reduced by more than 20% when comparing to the baseline heat 1 using only Inoculant-1. It is clear that Al can form inclusions that are capable of promoting the nucleation of the austenite during solidification. The detailed mechanism will be further investigated. The austenite liquidus recalescence was significantly decreased when Al was added to the melt. Attributed to the refined microstructure, UTS, yield strength and elongation of the material were improved compared to the baseline metal. More detailed inclusion analysis and graphite morphology study will be performed in the future work.

Conclusions

The effects of Ce/Ti/Al additions at various levels on the microstructure and mechanical properties of ductile iron were investigated in this research. It was concluded that there is a minimum required amount for Ce to refine the microstructure at thin section of ductile iron castings. For section size larger than a threshold, Ce was found not beneficial to the refinement of microstructure and elongation of ductile iron. Ti coarsens the microstructure in ductile iron castings, while the total nonmetallic inclusion density was reduced by 30%. Al was concluded effective in

Table 11. Liquidus Recalescence and Tensile Properties of Heats with Difference Al Additions

		Liquidus recalescence (°C)	UTS, ksi	Yield, ksi	Elong. %
Heat 1	Inoculant 1	0.33	105.82 ± 0.50	62.37 ± 0.67	9.92 ± 0.42
Heat 7	Inoculant 1 + 0.02 wt.% Al	<0.20	109.19 ± 0.24	61.70 ± 0.75	10.23 ± 0.55

refining the microstructure of ductile iron. When Al was added to the melt to achieve a residue amount of 0.02 wt.%, increases in tensile mechanical properties were achieved. Analysis of nonmetallic inclusions found in the matrix also indicated that additions change the composition and the type of inclusions, which may impact the tensile properties of DI. Future study will be investigating the interactions of additions with DI and influences on microstructure.

Acknowledgement

This paper is an invited submission to IJMC selected from presentations at the 7th Keith Millis Symposium on Ductile Iron held October 18–20, 2023, at the Crown Plaza Atlanta Perimeter at Ravinia, Atlanta, GA. It is published in the IJMC by permission of the DIS (Ductile Iron Society). The authors would like to thank the Ductile Iron Society for sponsoring this research project. Dura-bar, Miller and Company, Elkem and Carolina Metal Casting are acknowledged for providing the charge materials. Kramer Pursell at Metal Technologies was appreciated for assisting with the tensile testing. Fellow undergraduate research assistants at Georgia Southern University, Noah Brack, Audrey Lowery, were thanked for their efforts with conducting experiments and preparing sample.

REFERENCES

1. N.S. Tiedje, Specification and selection of ductile irons. Cast Iron Sci. Technol. (2017). https://doi.org/10.31399/ASM.HB.V01A.A0006325
2. R.C. Voigt, Patterns and patternmaking. Casting (2008). https://doi.org/10.31399/ASM.HB.V15.A0005308
3. A. Diószegi, P. Svidró, Volumetric changes during the solidification of cast iron. Cast Iron Sci. Technol. (2017). https://doi.org/10.31399/ASM.HB.V01A.A0006330
4. L.A. Mampuru, M.G. Maruma, J.S. Moema, Grain refinement of 25 wt% high-chromium white cast iron by addition of vanadium. J. South. Afr. Inst. Min. Metall. **116**, 969–972 (2016). https://doi.org/10.17159/2411-9717/2016/V116N10A12
5. D.M. Stefanescu, R. Ruxanda, The liquid state and principles of solidification of cast iron. Cast Iron Sci. Technol. (2017). https://doi.org/10.31399/ASM.HB.V01A.A0006311
6. X. Li et al., The effects of prior austenite grain refinement on strength and toughness of high-strength low-alloy steel. Metals **12**, 28 (2021). https://doi.org/10.3390/MET12010028
7. D.M. Stefanescu, Microstructure evolution during the liquid/solid transformation in cast iron. Cast Iron Sci. Technol. (2017). https://doi.org/10.31399/ASM.HB.V01A.A0006304
8. M. Ohno, K. Matsuura, Refinement of As-cast austenite microstructure in S45C steel by titanium addition. ISIJ Int. **48**, 1373–1379 (2008). https://doi.org/10.2355/ISIJINTERNATIONAL.48.1373.10.2355/ISIJINTERNATIONAL.48.1373
9. Y. Ji, M.X. Zhang, H. Ren, Roles of lanthanum and cerium in grain refinement of steels during solidification. Metals **8**, 884 (2018). https://doi.org/10.3390/MET8110884
10. X. Zhi, J. Liu, J. Xing, S. Ma, Effect of cerium modification on microstructure and properties of hypereutectic high chromium cast iron. Mater. Sci. Eng. A **603**, 98–103 (2014). https://doi.org/10.1016/J.MSEA.2014.02.080
11. D.M. Stefanescu, R. Ruxanda, Solidification structures of steels and cast irons. Metallogr. Microstruct. (2004). https://doi.org/10.31399/ASM.HB.V09.A0003725
12. W. Wang, P.D. Lee, M. McLean, A model of solidification microstructures in nickel-based superalloys: predicting primary dendrite spacing selection. Acta Mater. **5**, 12971–12987 (2003). https://doi.org/10.1016/S1359-6454(03)00110-1
13. Y. Ruan, H. Zhu, Q. Wang, F. Dai, D. Geng, B. Wei, Dendrite growth and micromechanical properties of rapidly solidified ternary Ni-Fe-Ti alloy. Prog. Nat. Sci. Mater. Int. **27**, 635–639 (2017). https://doi.org/10.1016/J.PNSC.2017.09.004
14. L. Winardi, C.R. Loper Jr., Influence of bismuth addition on primary austenite dendrite in gray cast iron. AFS Trans. **112**, 723–742 (2004)
15. D.M. Stefanescu, R. Ruxanda, Fundamentals of solidification. Metallogr. Microstruct. (2004). https://doi.org/10.31399/ASM.HB.V09.A0003724
16. M.A. Sheikh, J. Iqbal, Effect of lanthanum on nodule count and nodularity of ductile iron. J. Rare Earths **25**, 533–536 (2007). https://doi.org/10.1016/S1002-0721(07)60557-2
17. E. Fras, M. Górny, H.F. López, Eutectic cell and nodule count in cast iron part I. Theoretical background. ISIJ Int. **47**, 259–268 (2007). https://doi.org/10.2355/ISIJINTERNATIONAL.47.259
18. K.M. Pedersen, N.S. Tiedje, Graphite nodule count and size distribution in thin-walled ductile cast iron. Mater Charact **59**, 1111–1121 (2008). https://doi.org/10.1016/J.MATCHAR.2007.09.001
19. C. Liu et al., Effects of graphite nodule count on mechanical properties and thermal conductivity of ductile iron. Mater. Today Commun. **31**, 103522 (2022). https://doi.org/10.1016/J.MTCOMM.2022.103522
20. Z. Adabavazeh, W.S. Hwang, Y.H. Su, Effect of adding cerium on microstructure and morphology of Ce-based inclusions formed in low-carbon steel. Sci.

Rep. **7**, 1–10 (2017). https://doi.org/10.1038/srep46503
21. L.N. Bartlett, B.R. Avila, Grain Refinement in lightweight advanced high-strength steel castings. Int. Metalcast **10**, 401–420 (2016). https://doi.org/10.1007/s40962-016-0048-0
22. M. Sasaki, K. Matsuura, K. Ohsasa, M. Ohno, Refinement of As-cast austenite grain in carbon steel by addition of titanium. ISIJ Int. **49**, 1362–1366 (2009). https://doi.org/10.2355/ISIJINTERNATIONAL.49.1362
23. U. Gürol, E. Karadeniz, O. Çoban, S.C. Kurnaz, Casting properties of ASTM A128 Gr. E1 steel modified with Mn-alloying and titanium ladle treatment. China Foundry **18**, 199–206 (2021). https://doi.org/10.1007/S41230-021-1002-1/METRICS
24. M. Górny, M. Kawalec, G. Sikora, E. Olejnik, H. Lopez, Primary structure and graphite nodules in thin-walled high-nickel ductile iron. Cast. Metals **2018**(8), 649 (2018). https://doi.org/10.3390/MET8080649
25. M. Gelfi, D. Gorini, A. Pola, G.M. La Vecchia, Effect of titanium on the mechanical properties and microstructure of gray cast iron for automotive applications. J. Mater. Eng. Perform. **25**, 3896–3903 (2016). https://doi.org/10.1007/S11665-016-2227-9/METRICS
26. S.N. Lekakh, Effect of nonmetallic inclusions on solidification of inoculated spheroidal graphite iron. Int. Metalcast **13**, 47–57 (2019). https://doi.org/10.1007/s40962-018-0243-2
27. S.N. Lekakh, R. O'Malley, M. Emmendorfer, B. Hrebec, Control of columnar to equiaxed transition in solidification macrostructure of austenitic stainless steel castings. ISIJ Int. (2017). https://doi.org/10.2355/ISIJINTERNATIONAL.ISIJINT-2016-684
28. D.A. Arvola, M.C. Emmendorfer, R.J. O'Malley, S.N. Lekakh, L.N. Bartlett, Effect of grain refining on properties of a cast superaustenitic stainless steel. JMEP **28**, 1382–1390 (2019). https://doi.org/10.1007/S11665-019-03895-6